

## THREE-DIMENSIONAL DIRECT NUMERICAL SIMULATION OF SHOCK-INDUCED BUBBLE COLLAPSE NEAR GELATIN

J. W. J. Kaiser<sup>\*</sup>, S. Adami<sup>†</sup>, N. A. Adams<sup>‡</sup>  
 Technical University of Munich  
 Department of Mechanical Engineering  
 Chair of Aerodynamics and Fluid Mechanics  
 Boltzmannstraße 15, 85748 Garching, Germany

### ABSTRACT

We present fully three-dimensional numerical simulation results of shock-induced bubble collapse near a water-gelatin interface. We study how the incoming pulse form and its amplitude affect the dynamics of bubble collapse and the subsequent gelatin penetration. Three immiscible fluids (water, air, and gelatin) are considered, separated by a sharp interface (level set). A conservative interface-interaction model determines the exchange of momentum and energy. A block-structured multiresolution scheme is used to adapt the mesh to the evolving flow field.

Validation simulations (free-field bubble collapse, bubble collapse near a rigid wall) show that our numerical setup accurately predicts bubble collapse dynamics and post-collapse wave dynamics. Two-dimensional simulations assuming cylindrical symmetry reveal a quasi-self-similar collapse behavior of the bubble for each wave form. The gelatin-penetration dynamics are self-similar, too, and occur in three stages. The onset of the gelatin penetration is governed by the post-shock momentum after the bubble collapse. This is followed by a fast penetration upon the impact of the water hammer. The penetration rate slows down once interfacial instabilities grow at the water-gelatin interface.

Our three dimensional simulation results confirm the two-dimensional cylindrically-symmetric results of a single-bubble collapse. The collapse of two equi-sized bubbles results in a change of direction of the emitted water hammers. For our setup, the water hammers are deflected in the direction of the second bubble, and therefore impinge on the gelatin interface obliquely. The actual direction depends on the initial bubble separation distance and the stand-off distance from the interface, and will be further investigated in future work.

### INTRODUCTION

The cavitation of microbubbles plays an increasingly important role in therapeutic applications in modern medicine (Stride *et al.*, 2010). It occurs, for example, in non-invasive methods for treating kidney stones, and has been applied in approaches for improved cancer treatment or drug delivery (Coussios & Roy, 2008). When the bubble collapses, it emits a high-pressure shock wave and a high-velocity water hammer, which interact with the nearby tis-

sue. The emitted shock wave is thereby multiple orders of magnitude stronger than the initial wave which initiated the bubble collapse. Both effects can potentially rupture nearby tissue. The exact mechanisms, however, are yet unclear and motivate our numerical simulations.

Shock-induced bubble collapse near rigid and soft walls has been extensively investigated with a variety of numerical methods. For rigid walls, many investigations have been limited to two dimensions (Johnsen & Colonius, 2009, e.g.) or axisymmetric descriptions. Up to now, only few detailed fully three-dimensional simulations have been performed (Hawker & Ventikos, 2012, e.g.). For soft walls, mainly axisymmetric problems have been considered to reduce the complexity of the setup (Freund *et al.*, 2009; Kobayashi *et al.*, 2011; Pan *et al.*, 2018). Also, only few fully three-dimensional simulation results are available (Coralic & Colonius, 2013).

In this work, we investigate bubble collapse dynamics and gelatin interface deformation using fully three-dimensional numerical simulations. The simulations are performed with a block-structured multiresolution framework using sharp interface capturing (level-set) and low-dissipative shock capturing. Different from previous work (Adami *et al.*, 2016; Pan *et al.*, 2018), we consider other wave forms of the initial pressure pulse to better represent realistic pulses from medical applications. Besides the effect of the pressure magnitude, we vary the form of the pressure pulse and consider tensile parts after the actual positive pulse. Finally, we simulate the collapse of two bubbles with varying stand-off distances from the interface.

### NUMERICAL MODEL

#### Governing Equations and Discretization

The compressible Euler equations

$$\begin{aligned} \frac{\partial \rho}{\partial t} + \nabla^T \cdot \rho \mathbf{u} &= 0 \\ \frac{\partial \rho \mathbf{u}}{\partial t} + \nabla^T \cdot (\mathbf{u} \otimes \mathbf{u} + p \mathbf{I}) &= 0 \\ \frac{\partial \rho e}{\partial t} + \nabla^T \cdot ((\rho e + p) \mathbf{u}) &= 0 \end{aligned} \quad (1)$$

govern the motion of each fluid phase. Here,  $\rho$  is the density,  $\mathbf{u}$  the velocity vector,  $p$  the pressure,  $\mathbf{I}$  the identity tensor, and  $e$  the specific total energy. The set of equations is

<sup>\*</sup>jakob.kaiser@tum.de (Corresponding author)

<sup>†</sup>stefan.adami@tum.de

<sup>‡</sup>nikolaus.adams@tum.de

closed by the stiffened equation-of-state

$$p = (\gamma - 1)\rho e - \gamma p_\infty, \quad (2)$$

with the material parameters  $\gamma$  for the ratio of specific heats and  $p_\infty$  for the background pressure. We use  $\gamma = 1.4$  and  $p_\infty = 0$  for air,  $\gamma = 4.4$  and  $p_\infty = 6 \times 10^8$  Pa for water, and  $\gamma = 4.04$  and  $p_\infty = 6.1 \times 10^8$  Pa for gelatin.

We apply a finite-volume discretization scheme on cubic cells, with characteristic flux projection for the hyperbolic part (Roe, 1981) and global Lax-Friedrichs (GLF) flux splitting. Fluxes at cell faces are reconstructed from cell averages with the fifth-order WENO scheme (Jiang & Shu, 1996). The basic idea of WENO schemes is to apply low-dissipative, high-order stencils in smooth flow regions, while falling back to non-linear convex combinations of lower-order stencils in regions with large gradients. The governing equations are discretized in time with the third-order Runge-Kutta Total Variation Diminishing (TVD) time integration scheme (Gottlieb & Shu, 1998). The timestep size is limited by the CFL-condition

$$\Delta t = \text{CFL} \left( \sum_i \frac{\|u_i + c\|_\infty}{\Delta x_i} \right)^{-1} \quad (3)$$

with the speed of sound  $c$ , and the cell width in  $i$ -direction  $\Delta x_i$ ,  $i \in \{1, 2, 3\}$ . The CFL-number is set to  $\text{CFL} = 0.4$ .

We achieve efficient high-resolution simulations by applying a block-based multiresolution scheme, which adds grid points in flow regions with steep local gradients (Rossinelli *et al.*, 2011; Han *et al.*, 2014). It employs a tree-based data structure where cell-averaged data ( $\bar{U}$ ) on a refinement level  $l$  can be computed from level  $l+1$ , using the projection operator  $P_{l+1 \rightarrow l} : \bar{U}_{l+1} \rightarrow \bar{U}_l$ . Cell-averaged data on level  $l+1$  can be estimated from level  $l$ , using the prediction operator  $P_{l \rightarrow l+1} : \bar{U}_l \rightarrow \hat{U}_{l+1}$ . The details  $\bar{d}_{l,i} = \bar{U}_{l,i} - \hat{U}_{l,i}$  are the differences between predicted and cell-averaged data, and are used to determine the required resolution in space to achieve a given accuracy (Harten, 1995). If the details are larger than a pre-defined accuracy threshold, grid points are added. If the details are smaller, the current grid is sufficient to achieve the desired accuracy. For the three-dimensional simulations investigated in this work, an accuracy threshold of the relative error  $\epsilon_{l=l_{\max}} = 10^{-2}$  on the finest level  $l_{\max} = 3$  was found to be sufficient. A local timestepping approach further improves overall efficiency, by integrating each refinement level with its level-dependent timestep size. Accuracy and stability are maintained by adapting the timestep size after each full Runge-Kutta step on the finest level (Kaiser *et al.*, 2019).

### Sharp-interface Model

A level-set function  $\phi$  is employed to capture the fluid-fluid interfaces.  $\phi$  describes the signed distance between the cell center and the interface ( $|\nabla\phi| = 1$ ), and the zero-level-set ( $\phi = 0$ ) represents the interface. We solve the advection equation

$$\frac{\partial \phi}{\partial t} + \mathbf{u}_\phi \cdot \nabla \phi = 0 \quad (4)$$

to propagate the level-set field in time. The level-set advection velocity  $\mathbf{u}_\phi$  is obtained from the two-material Riemann problem at the interface, which is solved with a linearized Riemann solver (Saurel *et al.*, 2003). The signed-distance property  $|\nabla\phi| = 1$  is potentially violated when advecting the level-set field. Therefore, the level-set field is re-initialized after every full Runge-Kutta step by iterating the equation

$$\frac{\partial \phi}{\partial \tau} + \text{sign}(\phi_0) (|\nabla\phi| - 1) = 0 \quad (5)$$

in a pseudo time  $\tau$  to a steady state (Sussman *et al.*, 1994).

Cell-face fluxes close to the interface are reconstructed by introducing ghost cells across the interface (Fedkiw *et al.*, 1999). Ghost-cell states are obtained using a zeroth-order extrapolation of prime states  $\mathbf{q} = (\rho, \mathbf{u}, p)^T$  from the real fluid along the interface-normal vector  $\mathbf{n}_\Gamma = \nabla\phi / |\nabla\phi|$  by iterating the equation

$$\frac{\partial \mathbf{q}}{\partial \tau} - \mathbf{n}_\Gamma \cdot \nabla \mathbf{q} = 0 \quad (6)$$

to a steady state. Eq. (6) is solved for each fluid separately, and thus maintains the sharp-interface property of the method.

The exchange of momentum and energy across the interface is modeled by explicit interface exchange terms (Hu *et al.*, 2006). They are applied in each cell that is cut by the interface, and use the interface pressure and velocity from the two-material Riemann problem. Mass transfer across the interface is neglected.

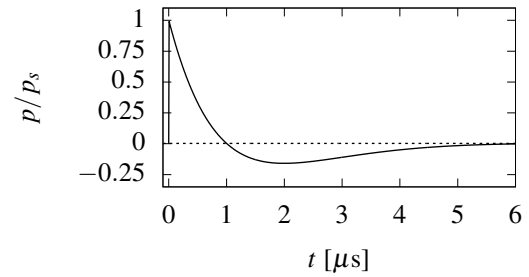


Figure 1. Pulse of a Dornier HM3 lithotripter (Church, 1989; Johnsen & Colonius, 2009).

### Pulse Waves and Simulation Setup

In this work, we compare the effect of two different waveforms on the collapse process and the subsequent gelatin deformation. Waveform 1 (WF1) is a planar shock wave, and waveform 2 (WF2) models the pulse of a Dornier HM3 lithotripter as

$$p(y) = p_0 + 2p_s e^{-\alpha t} \cos(\omega t + \pi/3) \quad (7)$$

with  $\alpha = 9.1 \times 10^5$  1/s and  $\omega = 2\pi \cdot 83.3$  kHz (Church, 1989; Johnsen & Colonius, 2009). Post-shock pressure and

velocity fields follow from the Rankine-Hugoniot conditions. The pulse form of eq. (7) is shown in Fig. 1.

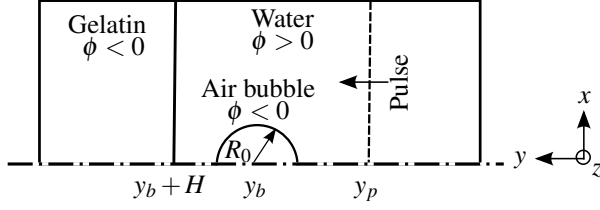


Figure 2. Initial configuration of the single-bubble simulations.

The initial condition is shown in Fig. 2 for a single-bubble simulation. The wave is initially located in the liquid far field, and impinges on the bubble at  $t = 0$ . The bubble has an initial diameter of  $R_0 = 100\mu\text{m}$ , and the stand-off distance between the bubble and the gelatin interface is  $H/R_0 = 2.0$ . Fig. 3 shows the setup for a multi-bubble simulation. The lateral distance between the two bubble centers is  $D/R_0 = 2.5$ . The stand-off distance to the interface is  $H/R_0 = 2$  for the downstream bubble, and the upstream bubble is shifted by  $\Delta H/R_0 = 1$ .

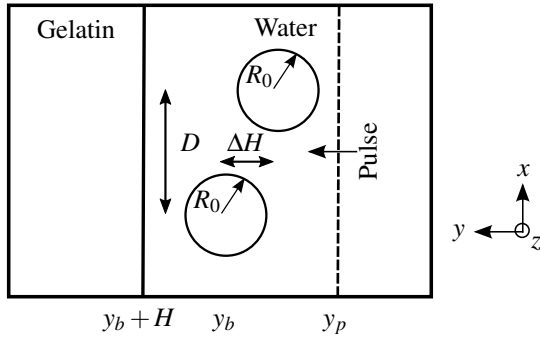


Figure 3. Initial configuration of the multi-bubble simulation.

## VALIDATION

### Rayleigh Collapse

We simulate the symmetric collapse of a spherical, non-condensable gas bubble in water and compare its collapse time to the theory of Rayleigh (1917). The Rayleigh collapse time  $t_c^R$  depends on the initial bubble radius  $R_0$ , the liquid density  $\rho_l$ , and the pressure inside the bubble  $p_g$  and in the liquid  $p_l$ . It is given by

$$t_c^R \approx 0.915 R_0 \sqrt{\frac{\rho_l}{p_l - p_g}} \quad (8)$$

(Brennen, 1995). We choose a quasi three-dimensional setup, and simulate only one half of the domain, assuming cylindrical symmetry. The bubble with radius  $R_0$  consists of air ( $\gamma = 1.4$ ) at atmospheric conditions ( $p_g = 10^5 \text{ Pa}$ ,  $\rho_g = 1.2 \text{ kg/m}^3$ ). We vary the pressure in the surrounding water ( $\gamma = 4.4$ ,  $p_\infty = 6 \times 10^8 \text{ Pa}$ ) to investigate the accuracy

of our setup. To avoid nonphysical initial conditions, the initial pressure field in the liquid satisfies the Laplace equation  $\Delta p_l = 0$ . The density field follows from the Rankine-Hugoniot conditions, assuming  $\rho = 998.6 \text{ kg/m}^3$  at ambient conditions. We choose a domain size of  $[40R_0 \times 40R_0]$ .

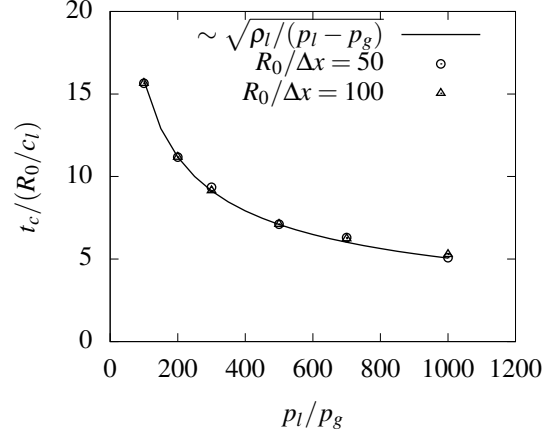


Figure 4. Normalized Rayleigh collapse time  $\tau_c/(R_0/c_l)$  for varying pressure ratios  $p_l/p_g$  for grid resolutions of  $R_0/\Delta x \approx 50$  ( $\odot$ ) and  $R_0/\Delta x \approx 100$  ( $\triangle$ ).

Fig. 4 shows the analytically expected behavior of the Rayleigh collapse time, and numerical solutions for two different resolutions  $R_0/\Delta x \approx \{50, 100\}$ , which are comparable to that used in the three-dimensional simulations. Results exhibit no grid dependency, and collapse times decrease with  $\sim \sqrt{\rho_l/(p_l - p_g)}$  as expected from literature. An offset of approximately 5% from the analytical results (eq. (8)) is observed in agreement with results from literature. In the following, we normalize our results with the free-field collapse time obtained from our simulation  $t_c^S \approx 0.973 R_0 \sqrt{\rho_l/(p_l - p_g)}$ .

### Bubble Collapse Near a Wall

As second validation case, we simulate the shock-induced collapse of a non-condensable gas bubble in water near a rigid wall to show that our model accurately reproduces post-collapse wave patterns. We use the simulation domain shown in Fig. 2, but replace the gelatin phase by a rigid wall with infinite acoustic impedance. The pressure-pulse profile is taken from eq. (7), with a pulse strength of  $p_s = 35 \text{ MPa}$ .

For this setup, Johnsen & Colonius (2009) have shown that the radial maximum pressure distribution along the wall follows

$$\frac{p_w}{p_s} \left( \frac{r}{R_0} \right) = \frac{c_1}{\sqrt{H_c^2 + (r/R_0)^2}} + c_2 \quad (9)$$

with the normalized collapse distance  $H_c$ , and calibration parameters  $c_1$  and  $c_2$ . A time series of radial pressure profiles along the wall is given in Fig. 5, together with eq. (9) using  $H_c = 1.5$ ,  $c_1 = 0.27$ , and  $c_2 = 0.022$ . The time difference between two radial pressure profiles is approximately  $\Delta t \approx 0.07 t_c^S$ . The temporal behavior of the maximum wall

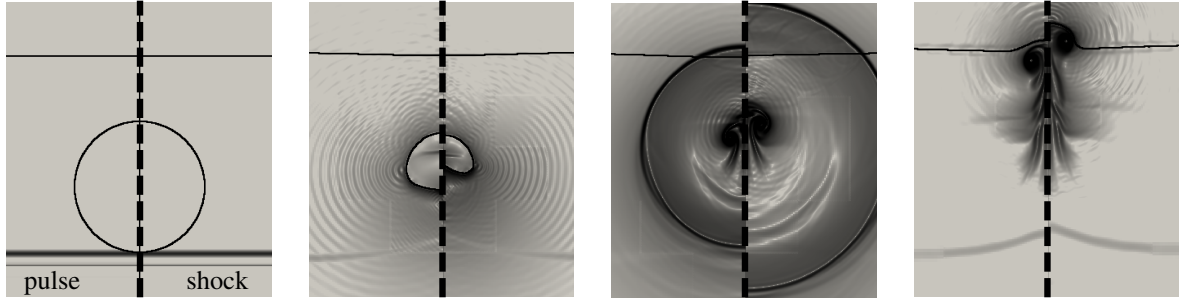


Figure 6. Numerical schlieren images of the two-dimensional simulation. The left half of each figure shows results for a  $p_s = 35$  MPa pulse wave, the right half for a shock wave of same strength. Flow direction is from bottom to top. Time instants are  $t/t_c^S = \{0, 0.95, 1.24, 1.94\}$ .

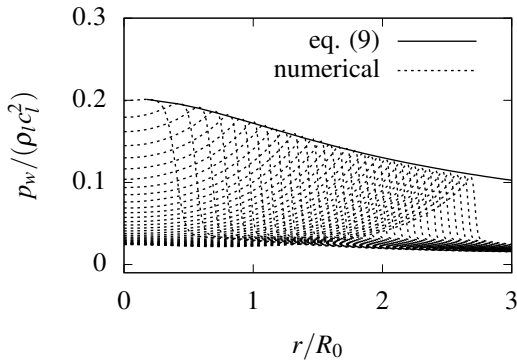


Figure 5. Normalized wall pressure in radial direction: empirical solution (solid), and numerical data (dotted), with  $\Delta t \approx 0.07t_c^S$  between two subsequent numerical profiles.

pressure agrees well with the empirical equation. It reproduces both the maximum-pressure peak near the centerline and the following radial decay.

## TWO-DIMENSIONAL SIMULATIONS

We present two-dimensional simulation results for bubble collapse and analyze the penetration depth of the gelatin interface. We simulate the domain as shown in Fig. 2.

Numerical schlieren images for a lithotripter pulse (left half) and a shock wave (right half) with identical strength  $p_s = 35$  MPa are shown in Fig. 6, at instants  $t/t_c^S = \{0, 0.95, 1.24, 1.94\}$ . The wave interacts with the bubble at  $t/t_c^S = 0$ . The bubble collapses faster after shock wave exposure ( $t/t_c^S = 0.95$ ) due to the higher energy density of the shock. Consequently, also the water hammer and the emitted shock wave occur earlier. The wave then propagates towards the gelatin interface, where it is completely transmitted since acoustical impedances of water and gelatin match for the chosen material parameters ( $t/t_c^S = 1.24$ ). The post-shock conditions cause the gelatin interface to migrate away from the bubble. The water hammer then penetrates the gelatin interface and leads to a strong deformation near the centerline ( $t/t_c^S = 1.94$ ).

Fig. 7 shows the equivalent bubble radius for wave forms 1 and 2, at different pulse strengths of 35 MPa and 70 MPa. The temporal behavior of the equivalent bubble radius yields quasi self-similar behavior for each waveform. For  $H/R_0 = 2$ , we obtain the relation  $t_c \approx 1.003 \cdot t_c^S$  for the shock wave induced collapse, and  $t_c \approx 1.077 \cdot t_c^S$  for the

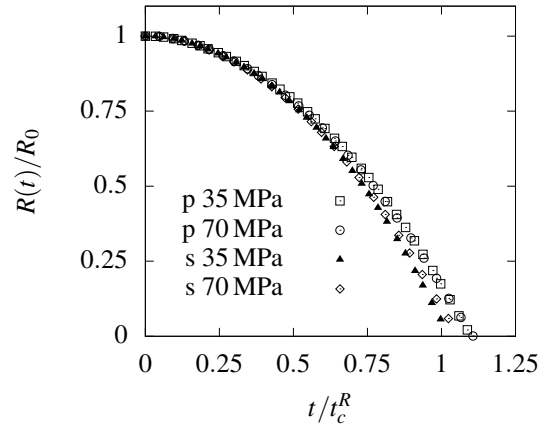


Figure 7. Equivalent bubble radius for different pulse (p) and shock (s) waves and strengths.

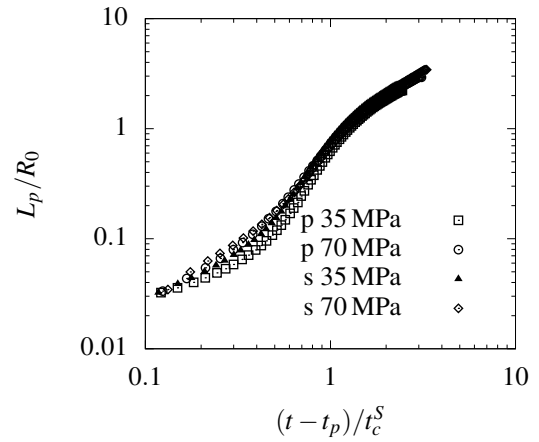


Figure 8. Penetration depth of the gelatin interface for different pulse (p) and shock (s) waves and strengths.

pulse wave induced collapse. Note, no rebound is visible, since the bubble becomes underresolved during the collapse and is removed explicitly as underresolved structure by the numerical method. The non-dimensional penetration depth is shown in Fig. 8. Here,  $t_p$  denotes the onset of penetration, i.e. when the interface starts moving in flow direction after the impact of the shock wave emitted by the collapsing bubble (Pan *et al.*, 2018). Three distinct regimes are observed, caused by different effects of the collapsing bubble.

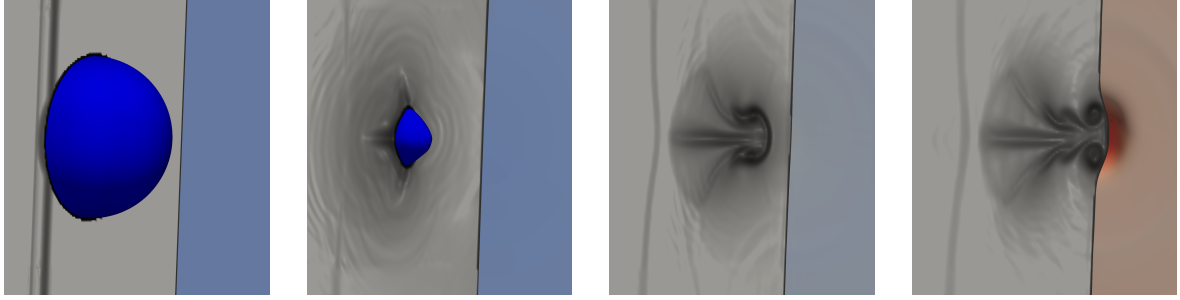


Figure 9. Isosurfaces and numerical schlieren images on the central  $x$ - $y$  plane of a single collapsing bubble at  $t/t_c^S = \{0.01, 0.64, 1.24, 1.94\}$ , simulated with a fully three-dimensional setup. Shock direction is from left to right. The bubble is shown in dark blue. The color scale of the gelatin interface indicates the displacement in shock direction.

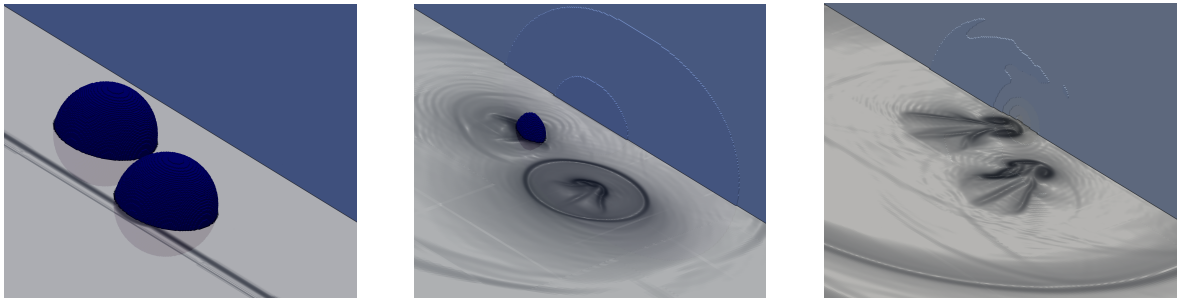


Figure 10. Isosurfaces and numerical schlieren images on the central  $x$ - $y$  plane of two collapsing bubbles at  $t/t_c^S = \{0.01, 1.21, 1.91\}$ . Shock direction is from left to right. The bubbles are shown in dark blue. The color scale of the gelatin interface indicates the displacement in shock direction.

The first, slow penetration regime results from the induced velocity behind the shock wave, which is emitted by the collapsing bubble. The water hammer impacts afterwards, and drastically increases the penetration rate. It slows down again once interfacial instabilities at the water-gelatin interface grow, which is the third growth regime. The second and third regime have already been reported by Pan *et al.* (2018), who investigated the collapse of a bubble without stand-off distance to the interface. For an attached bubble, the impact of the emitted shock wave and the water hammer coincide, thus the first scaling regime of our study is suppressed.

### THREE-DIMENSIONAL SIMULATIONS

#### Single-bubble collapse

As validation, we repeat the two-dimensional simulation for a 70MPa shock wave considering a fully three-dimensional setup.

Isosurfaces of the bubble and the gelatin interface, and numerical schlieren images in the central  $x$ - $y$  plane are shown in Fig. 9, at instants  $t/t_c^S = \{0.01, 0.64, 1.24, 1.94\}$ . The bubble is shown in dark blue, the color scheme of the gelatin interface indicates its displacement. The wave impinges on the bubble at  $t/t_c^S = 0$ , which initiates the collapse due to the sudden increase in the ambient pressure. While the bubble collapses, the gelatin interface is pulled towards the bubble ( $t/t_c^S = 0.64$ ). Once the bubble has collapsed, the interface moves in opposite direction due to the post-shock velocity ( $t/t_c^S = 1.24$ ). Then, the water hammer penetrates the gelatin interface ( $t/t_c^S = 1.94$ ). This behavior is in good qualitative agreement with our two-dimensional results.

#### Multi-bubble collapse

Finally, we investigate the collapse of two equi-sized bubbles near the gelatin interface. We extend the work of Pan *et al.* (2018) by breaking cylindrical symmetry and add a second bubble near the gelatin interface. The setup is sketched in Fig. 3.

Isosurfaces of the bubble and the gelatin interface, and numerical schlieren images in the central  $x$ - $y$  plane are shown in Fig. 9, at instants  $t/t_c^S = \{0.01, 1.21, 1.91\}$ . The bubbles are shown in dark blue, the color scheme on the gelatin interface indicates its displacement. For a single-bubble collapse, the circumferential pressure distribution around each bubble is symmetric to the centerline. For the multi-bubble collapse investigated here, the additional bubble breaks this symmetry ( $t/t_c^S = 1.21$ ). Therefore the water hammer generated by the collapse of the upstream bubble is deflected towards the downstream bubble. As the upstream bubble collapses earlier, the emitted shock wave propagates towards the downstream bubble, which is not yet collapsed. For the investigated distance between the two bubbles, this wave reaches the location of the downstream bubble only after the collapse, and therefore does not influence the collapse process itself. However, also the circumferential pressure field of the downstream bubble is influenced by the upstream bubble, which is why the water hammer emitted after the collapse is deflected towards the upstream bubble.

Considering the movement of the gelatin interface, an asymmetric, ellipsoidal distribution is observed at  $t/t_c^S = 1.21$ . The maximum deflection is located near the downstream bubble. After both bubbles have collapsed, the water hammers obliquely penetrate the gelatin interface ( $t/t_c^S = 1.91$ ).

## CONCLUSION

We have presented two- and three-dimensional simulation results of bubble-collapse scenarios near a tissue surrogate. We validated our setup with analytical and literature results, and performed simulations of the collapse of multiple bubbles near a soft wall (gelatin).

Our simulations reveal a quasi self-similar behavior of the gelatin penetration for single-bubble collapse with three distinct regimes. An initial slow penetration rate after the impact of the spherical shock wave is followed by a strong increase after the impact of the water hammer. The growth rate changes again once interfacial instabilities at the water-gelatin interface grow.

Three dimensional simulations of the collapse of two equi-sized gas bubbles were performed. The direction of the emitted water hammer is deflected compared to the single-bubble collapse, as the pressure field around each bubble is locally disturbed by the second bubble. The water hammers of the two bubbles therefore penetrate the gelatin obliquely, and potentially interact further downstream. For our setup, the collapse of the downstream bubble is not altered by the shock wave emitted after the upstream bubble collapsed. For a smaller distance, this wave potentially changes the collapse process of the downstream bubble, but further analyses are required.

The interaction between the two bubbles strongly affects the gelatin penetration. It is essential for a comprehensive understanding of the penetration process in real-life applications, where bubble clouds have to be considered. In addition, a more accurate representation of the gelatin phase is currently developed, taking into account for non-Newtonian material behavior.

## ACKNOWLEDGMENTS

The first author is supported by the German Research Foundation (Deutsche Forschungsgesellschaft, DFG). The second and third author acknowledge funding from the European Research Council (ERC) under the European Union's Horizon 2020 research and innovation program (grant agreement No. 667483). The authors gratefully acknowledge the Gauss Centre for Supercomputing e.V. (www.gauss-centre.eu) for funding this project by providing computing time on the GCS Supercomputer SuperMUC at Leibniz Supercomputing Centre (www.lrz.de).

## REFERENCES

Adami, S., Kaiser, J., Adams, N. A. & Bermejo-Moreno, I. 2016 Numerical modeling of shock waves in biomedicine. In *Center for Turbulence Research Proceedings of the Summer Program 2016*.

Brennen, C. E. 1995 *Cavitation and Bubble Dynamics*. Oxford engineering science series 44. New York: Oxford University Press.

Church, C. C. 1989 A theoretical study of cavitation generated by an extracorporeal shock wave lithotripter. *J. Acoust. Soc. Am.* **86** (1).

Coralic, V. & Colonius, T. 2013 Shock-induced collapse of a bubble inside a deformable vessel. *Eur. J. Mech. B/Fluids* **40**, 64–74.

Coussios, C. C. & Roy, R. A. 2008 Applications of Acoustics and Cavitation to Noninvasive Therapy and Drug Delivery. *Annu. Rev. Fluid Mech.* **40** (1), 395–420.

Fedkiw, R. P., Aslam, T. D., Merriman, B. & Osher, S. 1999 A Non-oscillatory Eulerian Approach to Interfaces in Multimaterial Flows (The Ghost Fluid Method). *J. Comput. Phys.* **152** (2), 457–492.

Freund, J. B., Shukla, R. K. & Evan, A. P. 2009 Shock-induced bubble jetting into a viscous fluid with application to tissue injury in shock-wave lithotripsy. *J. Acoust. Soc. Am.* **126** (5), 2746.

Gottlieb, S. & Shu, C.-W. 1998 Total variation diminishing Runge-Kutta schemes. *Math. Comput.* **67** (221), 73–85.

Han, L.H., Hu, X.Y. & Adams, N.A. 2014 Adaptive multi-resolution method for compressible multi-phase flows with sharp interface model and pyramid data structure. *J. Comput. Phys.* **262**, 131–152.

Harten, A. 1995 Multiresolution algorithms for the numerical solution of hyperbolic conservation laws. *Commun. Pure Appl. Math.* **48** (12), 1305–1342.

Hawker, N. A. & Ventikos, Y. 2012 Interaction of a strong shockwave with a gas bubble in a liquid medium: a numerical study. *J. Fluid Mech.* **701**, 59–97.

Hu, X.Y., Khoo, B.C., Adams, N.A. & Huang, F.L. 2006 A conservative interface method for compressible flows. *J. Comput. Phys.* **219** (2), 553–578.

Jiang, G.-S. & Shu, C.-W. 1996 Efficient implementation of weighted ENO schemes. *J. Comput. Phys.* **126**, 202–228.

Johnsen, E. & Colonius, T. 2009 Numerical simulations of non-spherical bubble collapse. *J. Fluid Mech.* **629**, 231.

Kaiser, J. W. J., Hoppe, N., Adami, S. & Adams, N. A. 2019 An adaptive local time-stepping scheme for multi-resolution simulations of hyperbolic conservation laws. Preprint submitted to *J. Comput. Phys.*

Kobayashi, K., Kodama, T. & Takahira, H. 2011 Shock wavebubble interaction near soft and rigid boundaries during lithotripsy: numerical analysis by the improved ghost fluid method. *Phys. Med. Biol.* **56** (19), 6421–6440.

Pan, S., Adami, S., Hu, X. & Adams, N. A. 2018 Phenomenology of bubble-collapse-driven penetratoin of biomaterial-surrogate liquid-liquid interfaces. *Phys. Rev. Fluids* **3**.

Rayleigh, L. 1917 VIII. On the pressure developed in a liquid during the collapse of a spherical cavity. *Philos. Mag.* **34** (200), 94–98.

Roe, P. L. 1981 Approximate Riemann solvers, parameter vectors, and difference schemes. *J. Comput. Phys.* **43** (2), 357–372.

Rossinelli, D., Hejazialhosseini, B., Spampinato, D. G. & Koumoutsakos, P. 2011 Multicore/multi-gpu accelerated simulations of multiphase compressible flows using wavelet adapted grids. *J. Sci. Comput.* **33** (2), 512–540.

Saurel, R., Gavriluk, S. & Renaud, F. 2003 A multiphase model with internal degrees of freedom: application to shock-bubble interaction. *J. Fluid Mech.* **495**, 283–321.

Stride, E. P., Coussios, C. C. & Wells, P. N. T. 2010 Cavitation and contrast: the use of bubbles in ultrasound imaging and therapy. *P. I. Mech. Eng. H* **224** (2), 171–191.

Sussman, M, Smereka, P. & Osher, S. 1994 A Level Set Approach for Computing Solutions to Incompressible Two-Phase Flow. *J. Comput. Phys.* **114**, 146–159.